JOURNAL OF PROPULSION AND POWER
Vol. 25, No. 3, May–June 2009

Experimental Study of a Mach 3 Bump-Compression Flowfield

Benjamin J. Tillotson,* Eric Loth,† and J. Craig Dutton‡
University of Illinois at Urbana–Champaign, Urbana, Illinois 61801
and
J. Mace§ and B. Haeffele¶
Boeing Phantom Works, St. Louis, Missouri 63166

DOI: 10.2514/1.35306

An experimental study has been conducted of the supersonic flowfield surrounding a bump-compression surface. The bump geometry is typical of that used to reduce the Mach number and boundary-layer thickness as part of an inlet system. The compression surface was mounted in a blowdown-type wind tunnel that was operated at a Mach number of 2.95 with a unit Reynolds number of 39×10^6 m^{-1}. Qualitative visualization of the flowfield included the use of oil streakline patterns to capture the surface-flow trends and schlieren photography to view shock waves and boundary-layer evolution along the bump surface. Static pressure measurements were obtained along the bump's centerline and at four spanwise planes. Along these same planes of investigation, laser Doppler velocimetry was used to provide mean velocity and turbulent stress distributions. The experiments showed that the bump induces a curved shock system originating from the leading edge of the compression surface without causing flow separation. The well-faired contour of the bump counteracts the initial pressure rise caused by the shock, yielding favorable pressure gradients in both the streamwise and spanwise-outward directions. These gradients push low-momentum boundary-layer fluid away from the model centerline to the sides of the bump. This results in a downstream boundary layer along the bump centerline that is thinner (by a factor of 2) and less turbulent than the incoming boundary layer.

I. Introduction

SUPERSONIC aircraft inlets are designed to capture and decelerate freestream air through a series of shock waves while minimizing the amount of low-momentum boundary-layer fluid on the inlet surfaces. High-Mach-number inlets often have an external compression surface that initiates the series of waves. Historically, the most common compression surface used for supersonic inlets has been a two-dimensional compression ramp. Hamed and Shang [1] presented a thorough discussion of supersonic inlet performance as it relates to inlet surfaces and their effects on flowfield turbulence, shock structure, and flow separation. This review presents excellent context for the concerns associated with inlet design and shows that there is room for improved performance. The current paper investigates a three-dimensional bump-compression surface that may have additional advantages in terms of thinner boundary layers for the flow that would enter the inlet.

The concept of a three-dimensional surface for use in supersonic inlet applications has been investigated before. Simon et al. [2] studied an external bump inlet in a direct comparison with a traditional two-dimensional compression ramp. It was determined that the bump inlet outperformed the 2-D ramp inlet over a range of Mach numbers from 1.5 to 2, whereby both surfaces employed boundary-layer bleed. The bump surface also provided satisfactory operational stability and proved to be relatively insensitive to yaw and angle-of-attack variation over the range of the study. Seddon and Goldsmith [3] described the bump intake as a novel device. They cited Ferri [4] as suggesting that a bump-compression surface could be formed by tracing fluid streamlines through the flowfield of a cone in supersonic flow and also noted that such a design was adopted for use in the Grumman Super-Tiger aircraft.

Gridley and Cahill [5] and Gridley and Walker [6] discussed the Advanced Compact Inlet System program, which was dedicated in part to the analysis of several fundamentally different compression systems. The bump inlet was one of the systems studied, and it was noted for its relatively simple design and the ability to operate without extensive boundary-layer management. It performed comparably with a 2-D waverider inlet while reducing weight, suffering from less drag, and maintaining ease of fabrication. Hamstra et al. [7,8] received patents for the design of a bump-inlet device called a diverterless supersonic inlet (DSI) [9,10]. The DSI was developed using the concept of conical streamline surface derivation, with advanced contouring of the bump shoulder leading to enhanced boundary-layer diversion. Bump inlets eventually went into use in the Joint Strike Fighter designs of both Lockheed Martin Corporation (the DSI) and The Boeing Company. However, there are no published studies that have made a detailed examination of the boundary-layer evolution and the associated shock interaction physics for supersonic bump flows. This information may be helpful for both improving the design of such bumps as well as to validate computational fluid dynamics methods for such flows and is the subject of the present study.

The goal of this investigation is to experimentally document the flowfield associated with a bump-compression surface in supersonic flow. Given the importance of maintaining a thin boundary layer with low turbulent stresses through the adverse pressure-gradient conditions typically encountered in supersonic inlet applications, the current paper will focus on the boundary layer's evolution as it traverses the bump. A comparison between the flow characteristics of a traditional two-dimensional compression ramp and that of the bump surface, both in the absence of boundary-layer management devices, is also included in this study. In a practical application, a single bump surface would be placed partially within the cowl of

Presented as Paper 11 at the 44th AIAA Aerospace Sciences Meeting and Exhibit, Reno, NV, 9–12 January 2006; received 6 November 2007; accepted for publication 22 December 2008.

*Currently Lockheed Martin Commercial Space Systems, Newtown, PA. Member AIAA.
†Professor and Associate Head, Aerospace Engineering Department, 104 South Wright Street. Associate Fellow AIAA.
‡Professor and Head, Aerospace Engineering Department, 104 South Wright Street. Associate Fellow AIAA.
§Technical Fellow, Propulsion and Thermodynamics Department, Mail Stop 0641231, Associate Fellow AIAA.
¶Engineer/Scientist, Propulsion and Thermodynamics Department, Mail Stop 0641231.

an inlet system in much the same way that more traditional compression ramps are used. Although the present fundamental flowfields are only qualitatively representative of the fluid dynamics occurring in actual ramp and bump inlets, the comparison between a simple ramp and bump flow may provide valuable insight. Furthermore, the authors are not aware of any previous study that has made such a detailed comparison between these two fundamental flowfields.

Figure 1 shows a schematic of the bump that was designed and fabricated by Boeing for the current study at the University of Illinois. It includes a smoothed ramp-up of the surface angle along the centerline to a maximum of about 10 deg. The cross section of the model is Gaussian-like in the spanwise direction. The bump leading edge is defined as the center of the pressure tap located along the model centerline at the point at which the bump surface begins to ramp up. The bump has a maximum height of approximately 10 mm and a maximum width of 64 mm at the trailing edge, which is located 123 mm from the leading edge. The downstream end of the bump is terminated by a flat surface angled down at approximately 18 deg. The bump-compression surface was mounted flush with the wind-tunnel floor.

II. Experimental Apparatus and Methods

A. Experimental Facility

The bump flowfield was investigated experimentally at the University of Illinois Gas Dynamics Laboratory. A blowdown wind tunnel with a 10.2 cm square test section was used for all experimentation. The tunnel operated at Mach 2.95 with a unit Reynolds number of 39×10^6 m^{-1}. The stagnation pressure was maintained at 414 kPa, with the stagnation temperature in the range of 300–303 K. Tunnel run times in excess of 6 min were possible, given these conditions. For all results discussions, x corresponds to the streamwise direction with positive values downstream of the bump leading edge, y corresponds to the transverse (wall-normal) direction with positive direction upward, and z corresponds to the spanwise direction with its origin located at the model centerline.

B. Measurement Methods

Schlieren photography and surface streakline visualization were used to observe the general flow features. The schlieren photographs were generated by a z-type mirror configuration with a 1.4-μs-duration light pulse from a Xenon model 457 Micropulser. The knife edge was oriented horizontally to cut off approximately half of the light and to accentuate vertical density gradients in the flow, thereby rendering the boundary layer more visible in the Polaroid black-and-white photographs. The surface streaklines were obtained by applying a mixture of ISO (International Organization for Standardization) 68-weight oil and talc to the model. The addition of talc to the oil made the streakline pattern visible on the model's dark anodized surface. This mixture had a viscosity that allowed it to follow the surface-flow pattern during tunnel operation and to maintain the pattern through shutdown. Static pressures were measured at 0.66-mm-diam taps along the model centerline and at four spanwise planes using vinyl tubing connected to Pressure Systems, Inc., model 9816 differential pressure modules. The pressure modules used for taps along the bump surface measure over the range of −103 to 103 kPa, and the stagnation-pressure module measures over the range of 0 to 689 kPa. These modules are quoted as being accurate to approximately ±0.038 kPa. A Setra model 370 digital pressure gauge, accurate to ±0.02 kPa, displayed the local atmospheric pressure. This value was added to the gauge pressures to determine absolute pressures.

A two-component, fiber-optic TSI laser Doppler velocimetry (LDV) system, coupled with a Stabilite model 2017 argon-ion laser, was used to determine streamwise and transverse mean flow velocities and turbulent stresses throughout the flowfield. The tunnel airflow was seeded in the stagnation chamber with silicone oil droplets, which were generated by a TSI six-jet atomizer. The droplets have a mean diameter of 0.8 μm. Previous studies [11] have shown that significant particle dynamics effects (deviations of more than 2% from the local fluid velocity) will only exist within 2–3 mm of the shock generated by the bump. Considering rotational alignment and equipment uncertainty as well as applying a postfacto interarrival-time weighting technique to account for velocity bias, the worst-case uncertainty in mean velocity for both measured components is estimated to be 2.1% of the freestream velocity (U_∞ = 625 m/s). The uncertainties in the fluctuating velocities were driven primarily by velocity gradients and estimated to be a maximum of 2.2% of the freestream velocity. Because the uncertainty in the fluctuating term is driven by velocity gradients, it is highest for the streamwise velocities near the wall in regions of high shear and becomes much less in the freestream or for the transverse velocities.

A variable-measurement density was used in the transverse direction, with data points closest to the bump spaced 0.1 mm apart and ranging up to 0.5 mm spacing in the freestream. The streamwise and transverse positioning are accurate to within 0.1 mm, and the spanwise location uncertainty is less than 1 mm. Nearest-to-the-wall velocity measurements in the incoming boundary layer were limited to approximately 1 mm and higher, due to beam clipping on the sides of the bump-model insert. Along the model centerline, where the bump surface is elevated, beam clipping was not an issue and measurements could be made to within 0.5 mm. However, glare issues prevented data collection below 1 mm for several offcenterline locations.

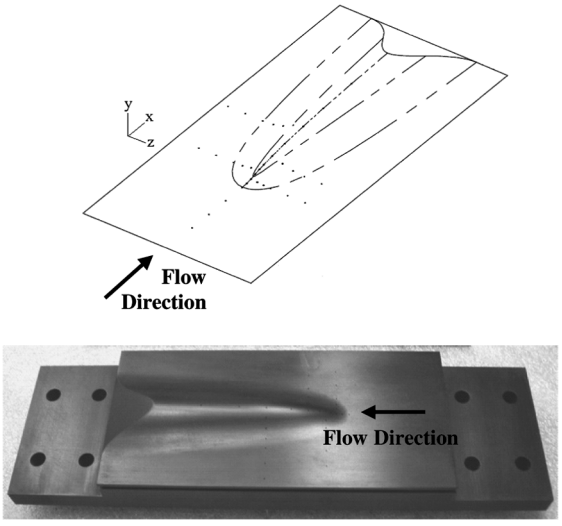

Fig. 1 Three-dimensional view and photograph of the Boeing bump-compression surface.

III. Experimental Results

A. Flow Visualization

The schlieren photograph of the bump flowfield shown in Fig. 2 provides qualitative insight into the bump's effects on the approach boundary layer. The approach boundary layer, seen as the dark region directly adjacent to the model, appears to be approximately as thick as the maximum height of the bump. As it encounters the bump surface, the uppermost extent of the boundary layer appears to remain at the same approximate transverse height, despite the fact that the bump height is increasing. This suggests that the downstream

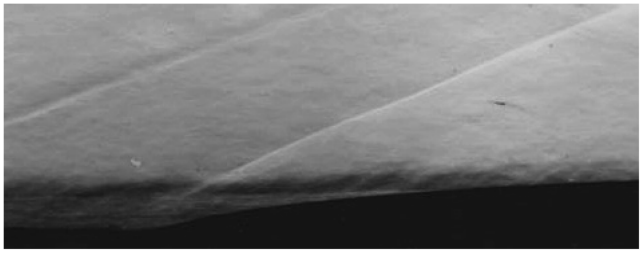

Fig. 2 Schlieren photograph of the bump flowfield.

boundary layer along the bump centerline has decreased in thickness relative to its incoming state. The other primary feature of the flowfield seen in the photo is the shock wave, evident as the bright white line that originates in the boundary layer near the bump leading edge and travels at a nearly constant angle through the flowfield. Although the shock appears to be oblique and planar in nature from this image, it actually wraps around the bump surface in a three-dimensional manner similar to a bow shock. A Mach wave originating upstream of the schlieren field of view can also be seen in Fig. 2. This weak wave is a result of a slight geometric mismatch at the point at which the flat portion of the bump-model insert meets the plane of the tunnel floor and has no appreciable impact on the studied flowfield.

Figure 3 shows the streakline pattern for the bump surface. The surface-flow results show no obvious evidence of separation and thus indicate that the flowfield is attached everywhere. It is also apparent from the outward deflection of streaklines that significant diversion of the flow exists in the spanwise direction, resulting in a highly three-dimensional flow near the surface. The general outline of the shock foot lies where the incoming parallel streaklines initially deflect outward.

B. Static Pressure Measurements

The static pressure taps, most of which can be seen in Fig. 1 as dots on the model surface, consist of one row of taps oriented in the streamwise direction along the bump centerline and four spanwise rows of taps. The first of these spanwise rows is located 7.6 mm downstream of the bump leading edge, with the successive rows spaced progressively further downstream at 14.7, 25.4, and 51.6 mm from the leading edge. The static pressure measurements along these lines of investigation are shown in Figs. 4 and 5. Referring to the centerline data (Fig. 4), a sharp rise in pressure to a ratio of $P/P_\infty = 1.6$ is seen across the shock at the leading edge of the bump, after which the pressure falls, indicating a favorable pressure gradient for the supersonic flow. With two-dimensional highly separated ramp flows, the shock system often sits upstream of the ramp corner and the compression process is marked by a plateaulike region of low compression through the separated region, with much steeper rises just upstream and downstream of the plateau. In the case of the bump, there is no significant shock standoff from the leading edge and the compression rise shows no plateau. This is further evidence of the absence of separation in the bump flowfield.

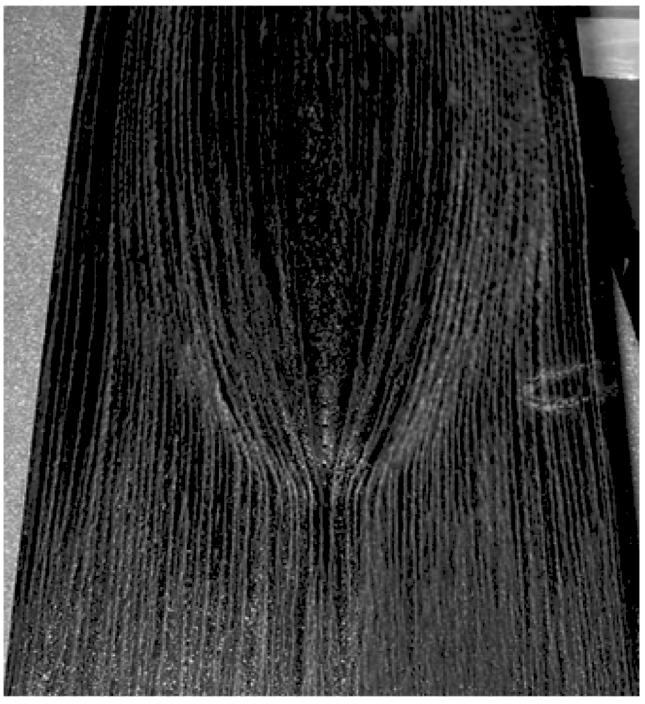

Fig. 3 Surface streakline pattern.

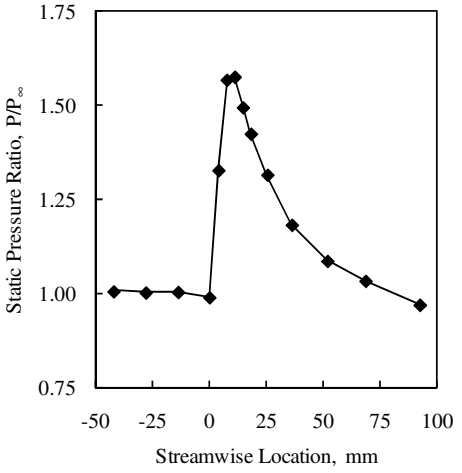

Fig. 4 Streamwise static pressure distribution.

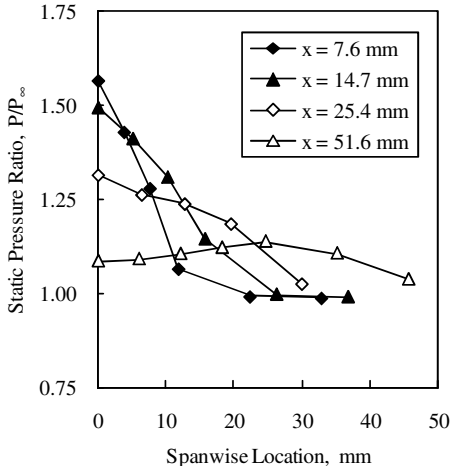

Fig. 5 Spanwise static pressure distributions.

The rise in centerline pressure is immediately followed by a substantial favorable pressure gradient. This favorable pressure gradient exists over essentially the entire remaining measured length of the bump, and at the last tap, the pressure has returned to the incoming freestream value. There is only negligible variation in pressure upstream of the bump leading edge, as expected.

The spanwise pressure profiles (Fig. 5) show considerable streamwise evolution. At the first three spans ($x = 7.6$, 14.7, and 25.4 mm), the maximum measured pressures occur at the model centerline. Additionally, at each successive downstream span, the maximum pressure decreases and is accompanied by an increased outward distribution of the region of compression. At the farthest downstream span ($x = 51.6$ mm), the maximum pressure occurs away from the model centerline. The spanwise pressure evolution is evidence of the spanwise diffusion of the bump-compression process, which is due to both the shock system and the well-faired geometry of the bump itself. The strong favorable spanwise-outward pressure gradients, combined with the centerline gradient, are primarily responsible for the substantial initial spanwise flow deflection on the bump surface seen just downstream of the leading edge (Fig. 3).

C. Mean Velocity and Turbulent Stress Measurements

The incoming boundary layer (42 mm upstream of the bump leading edge) was measured in detail to quantify the inflow condition and to ensure flow uniformity in the spanwise direction. The mean streamwise velocity u profiles from seven spanwise locations for this upstream position are shown in Fig. 6. These velocity profiles, as well as turbulent stress profiles not shown here, confirm spanwise uniformity of the flow. Both the mean and fluctuating velocity components were found to be typical of a fully developed,

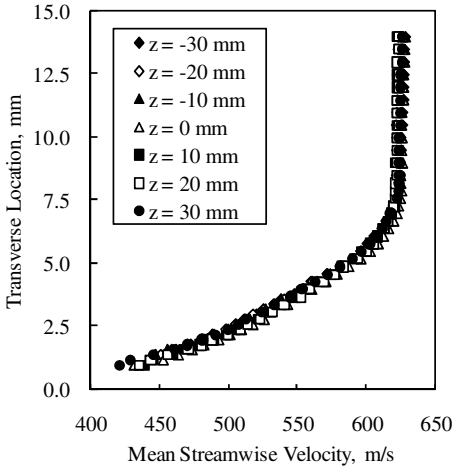

Fig. 6 Mean streamwise velocity profiles of the incoming boundary layer.

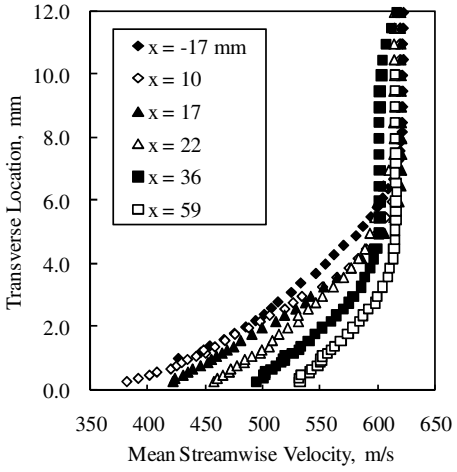

Fig. 8 Mean streamwise velocity profiles along the bump centerline.

two-dimensional, compressible turbulent boundary layer. A least-squares curve fit to the velocity distribution of Sun and Childs [12] was applied to these profiles, and it was determined that the incoming boundary-layer thickness δ was 7.7 mm. This and the freestream velocity of 625 m/s were used to generate the spanwise-averaged, nondimensional, incoming boundary-layer profile shown in Fig. 7.

Given the confirmation of spanwise uniformity of the inflow, LDV measurements along the length of the bump were made on only half of the span of the flowfield based on lateral symmetry. Data were acquired at approximately 1200 pointwise locations along the centerline plane of the bump. These included vertical surveys at 9 streamwise locations in the boundary layer upstream of the bump leading edge starting at $x = -42$ mm, 13 streamwise locations within the first 25 mm of the bump surface starting at the leading edge, and 8 more streamwise locations toward the aft end of the bump, with the furthest downstream location at $x = 84$ mm. At each streamwise station, the majority of the vertical measurement locations were concentrated close to the bump surface to capture the large spatial gradients in the boundary layer. Additional data were acquired in the freestream to quantify the extent of the shock wave's influence on the inviscid portion of the flowfield. Four spanwise measurement planes were investigated at the streamwise locations shown in Fig. 5, with each plane composed of approximately 240 individual spatial locations collected in line with the pressure taps. As with the centerline plane, measurement density was highest within the boundary layer for each of the spanwise grid locations.

Several mean streamwise velocity and streamwise normal stress profiles along the bump centerline are provided in Figs. 8 and 9. The mean streamwise velocity profiles show that the bump surface causes thinning of the boundary layer on the model centerline, which can be seen with the $x = 10$ and 17 mm profiles. In the boundary-layer region, the velocity profile becomes consistently more full from $x = 10$ mm onward due to the favorable pressure gradient (Fig. 4). However, the flow above the boundary layer shows a velocity reduction due to the oblique shock emanating from the bump leading edge, particularly for the $x = 22$ and 36 mm profiles. At the most downstream location ($x = 59$ mm), the boundary layer has thinned significantly due to the favorable pressure gradient, and the freestream velocity has recovered to approximately the incoming value because of the expansion waves developing from the curved bump surface. The streamwise normal stress profiles show an increase in turbulence behind the shock, as maximum stresses are clearly higher at the $x = 10$ and 17 mm profiles than in the incoming boundary layer. The turbulence begins to diminish past these locations due to the favorable pressure gradient, and at the last profile shown ($x = 59$ mm), the maximum stresses have decreased significantly.

Contour plots of the entire set of centerline mean velocity and turbulent stress data are shown in Fig. 10. This figure supplements the selected profiles of Figs. 8 and 9 and provides a more global view of the centerline flowfield plane. The mean streamwise velocity is consistent with the features shown in the schlieren photograph, in that the boundary-layer thickness decreases over the length of the bump. There is also a region of slight flow retardation just downstream of the shock wave, as was observed with the individual velocity profiles. The mean transverse velocity v shows strong flow deflection immediately behind the shock, followed by a gradual realignment of the flow in the streamwise direction.

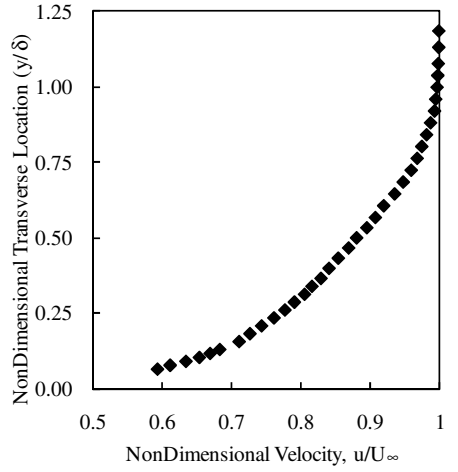

Fig. 7 Nondimensional spanwise-averaged incoming mean velocity profile.

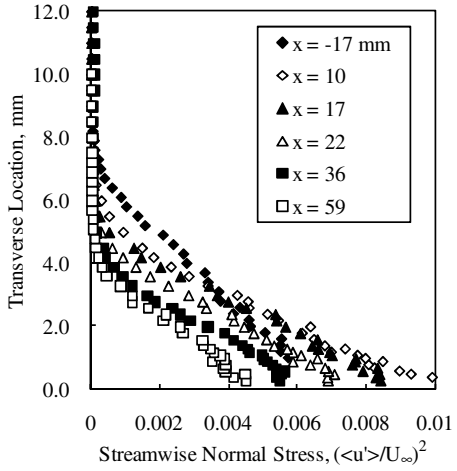

Fig. 9 Streamwise normal stress profiles along the bump centerline.

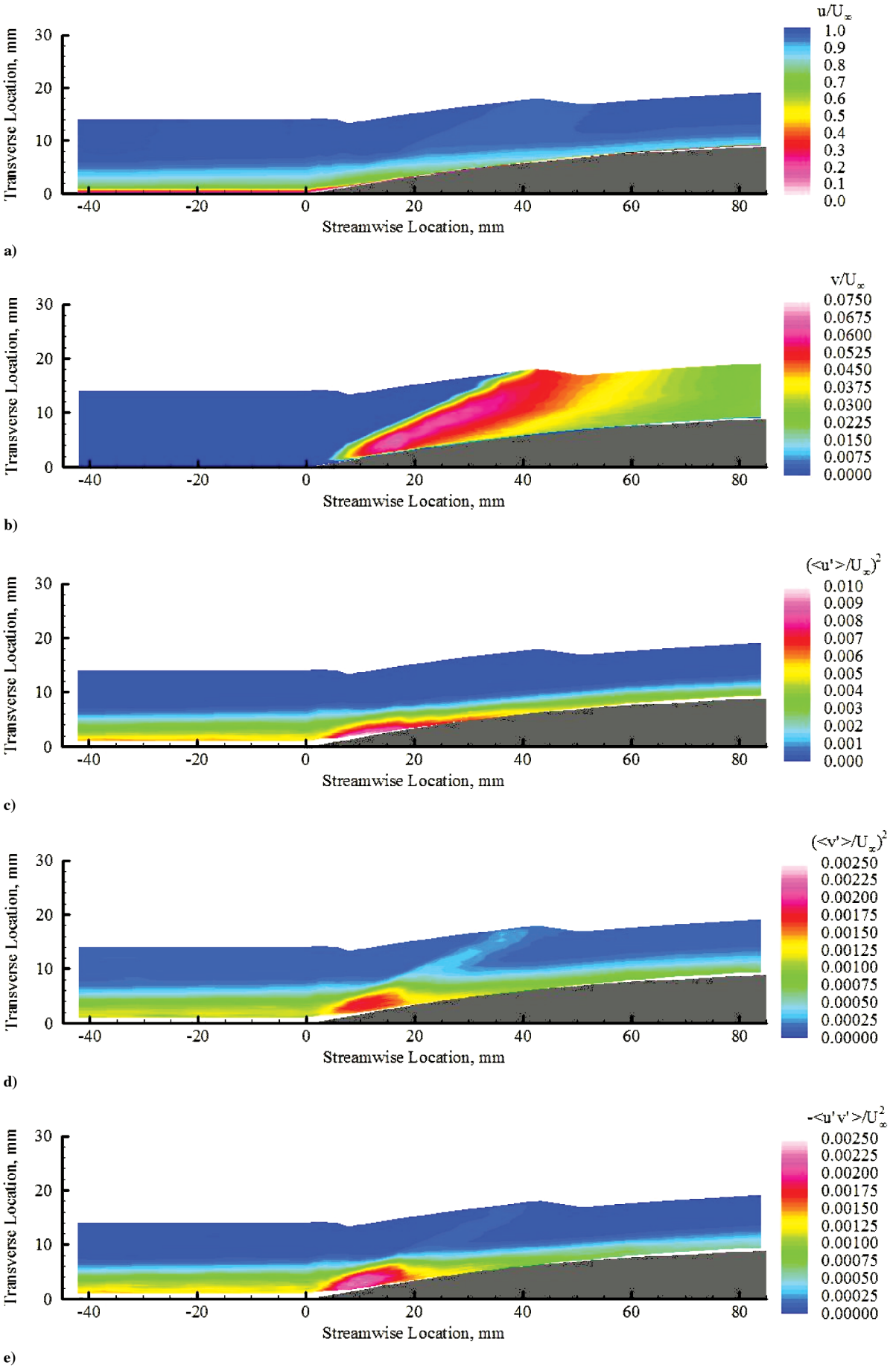

Fig. 10 Centerline plane results: a) mean streamwise velocity, b) mean transverse velocity, c) streamwise normal stress, d) transverse normal stress, and e) shear stress.

All three measured turbulent stress components undergo a substantial rise in the vicinity of the shock before decreasing to levels slightly below that of the incoming boundary layer. This behavior is effectively the result of counteracting phenomena. The initial disturbance is the strong compression caused by the shock wave, which increases turbulence levels. This is immediately followed by spanwise flow deflection and expansion along the bump centerline, which yields a thinner, less turbulent, downstream boundary layer. The turbulent stresses are highly anisotropic throughout the measurement region, with the streamwise normal stress being, by far, the largest component. The lighter blue bands in the freestream region corresponding to the shock location in Figs. 10d and 10e are areas of slight measured velocity fluctuations in the freestream in the neighborhood of the shock. These can be attributed to slight shock unsteadiness (noticed when comparing several instantaneous images of the flow) and polydispersion of the

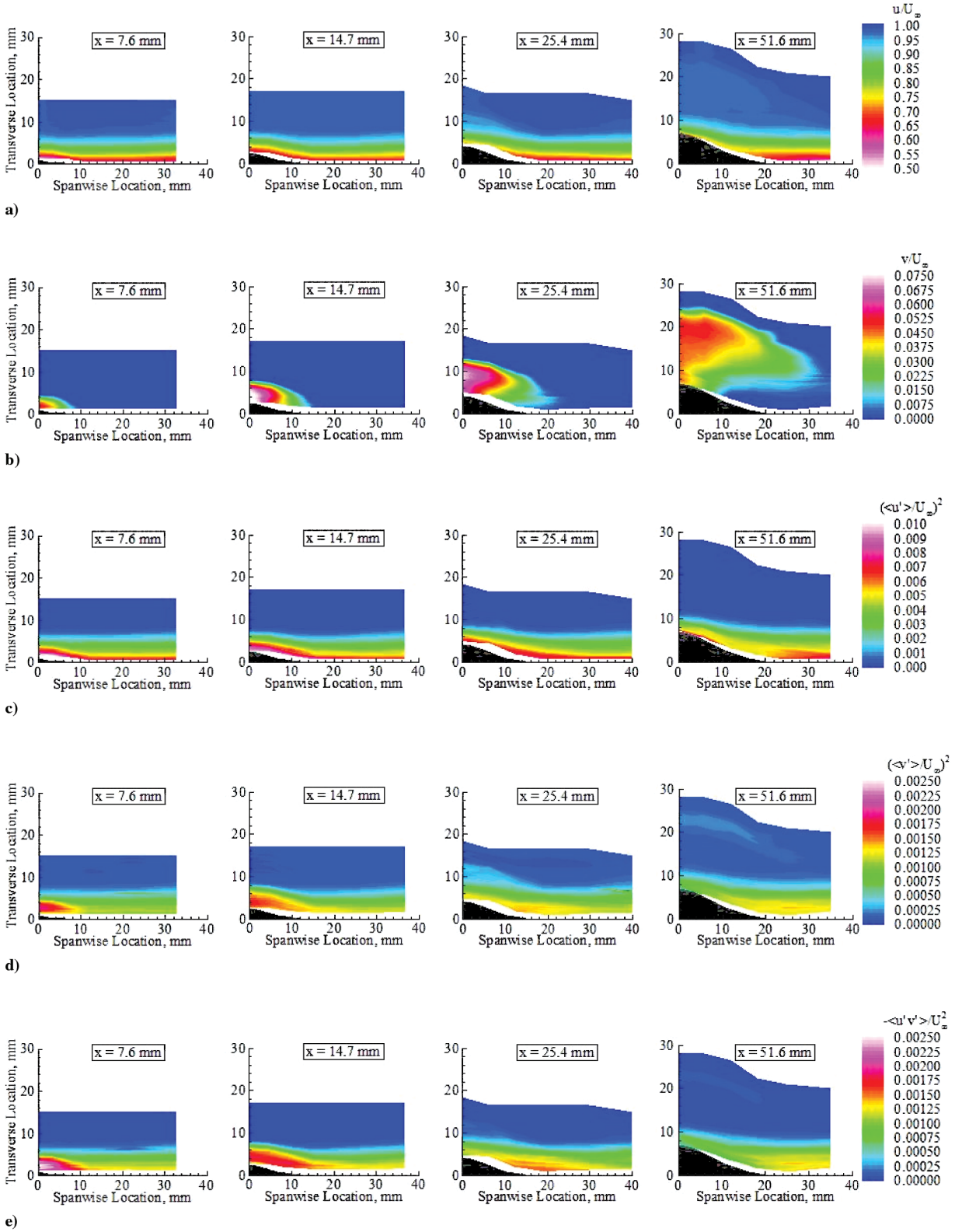

Fig. 11 Spanwise plane results: a) mean streamwise velocity, b) mean transverse velocity, c) streamwise normal stress, d) transverse normal stress, and e) shear stress.

atomized seed droplets (because the random appearance of somewhat larger droplets may require 2–3 mm to fully accommodate to the postshock flow velocity field).

The spanwise plane mean velocity and turbulent stress results are summarized in Fig. 11. The streamwise mean velocity figures show that the favorable streamwise and spanwise-outward pressure gradients transfer low-momentum boundary-layer fluid further away from the bump centerline at each successive downstream span. The transverse mean velocity again shows substantial flow deflection, with the basic envelope of the shock system increasing in physical dimension at each successive measured span. Peak levels of streamwise normal stress remain significant along the model centerline at the farthest downstream spans. However, the region of highly turbulent fluid is significantly thinned along the centerline, with a corresponding increase in the size of the turbulent regions to the side of the bump. Both the transverse normal stress and shear stress develop pockets of high values around the model centerline at the first span investigated. This region of highly turbulent fluid spreads outward at successive spans and eventually completely off to the sides of the bump. Unlike the streamwise normal stress, neither the transverse normal nor shear stresses retain a region of high turbulence along the model centerline at the downstream locations.

Individual mean streamwise velocity profiles, such as those shown in Fig. 8, were evaluated to quantify boundary-layer thickness evolution over the bump surface. A simple estimation of the boundary-layer thickness $\delta_{0.98}$ for each profile was made by determining the y location at which the mean streamwise velocity attains 98% of the freestream value. This was done by linearly interpolating between the discrete y locations that bound the 98% freestream velocity value, and it is estimated that this method is accurate to within 10% of the boundary-layer height. The centerline boundary-layer evolution is provided in Fig. 12. Upstream of the bump leading edge, the boundary layer experiences some natural growth. However, immediately downstream of the shock, the boundary layer begins to dramatically decrease in thickness, which is a direct result of the favorable pressure gradient shown in Fig. 4. Approximately 50 mm downstream of the bump leading edge, the boundary layer appears to asymptote to a thickness that is less than half of the incoming value. This decrease in centerline boundary-layer thickness is accompanied by an increase of the spanwise-outer boundary-layer thickness, as shown in Fig. 13. Again, this behavior is expected due to the spanwise pressure gradients seen in Fig. 5. The evolution of the boundary layer from being slightly thicker than the centerline value at outward spanwise locations at $x = 7.6$ mm to a drastic outward increase at $x = 51.6$ mm is readily apparent.

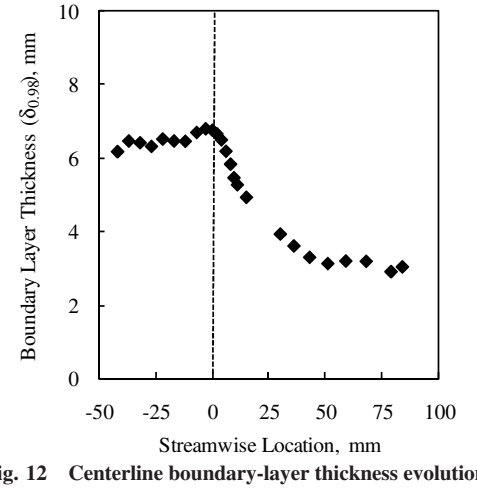

Fig. 12 Centerline boundary-layer thickness evolution.

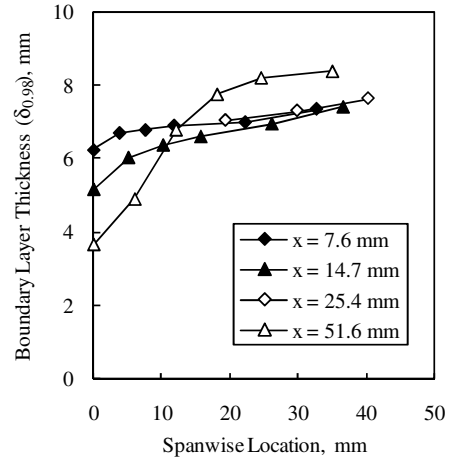

Fig. 13 Spanwise boundary-layer thickness evolution.

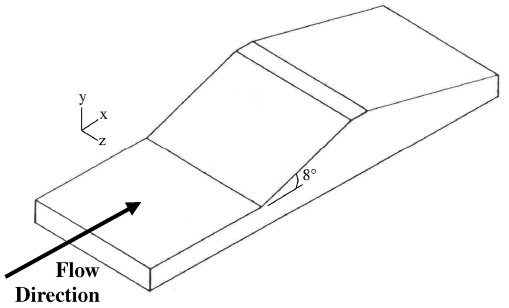

Fig. 14 Kuntz [13] two-dimensional compression-ramp model.

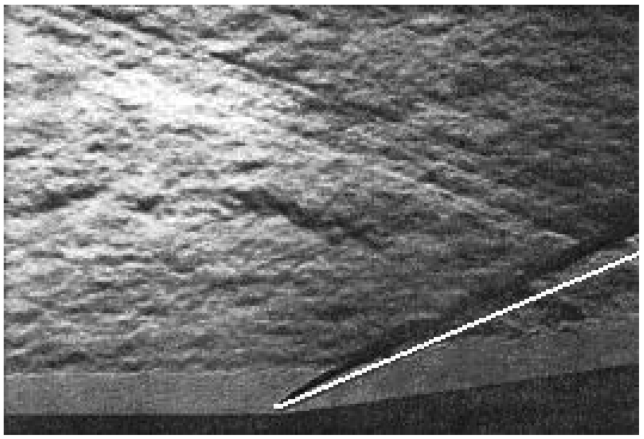

Fig. 15 Schlieren photograph of a Kuntz [13] 8 deg ramp flowfield with bump shock angle shown in white.

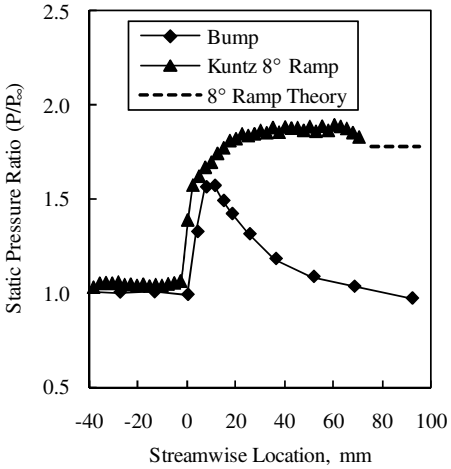

Fig. 16 Static pressure comparison of a Kuntz [13] 8 deg ramp with bump-compression surface.

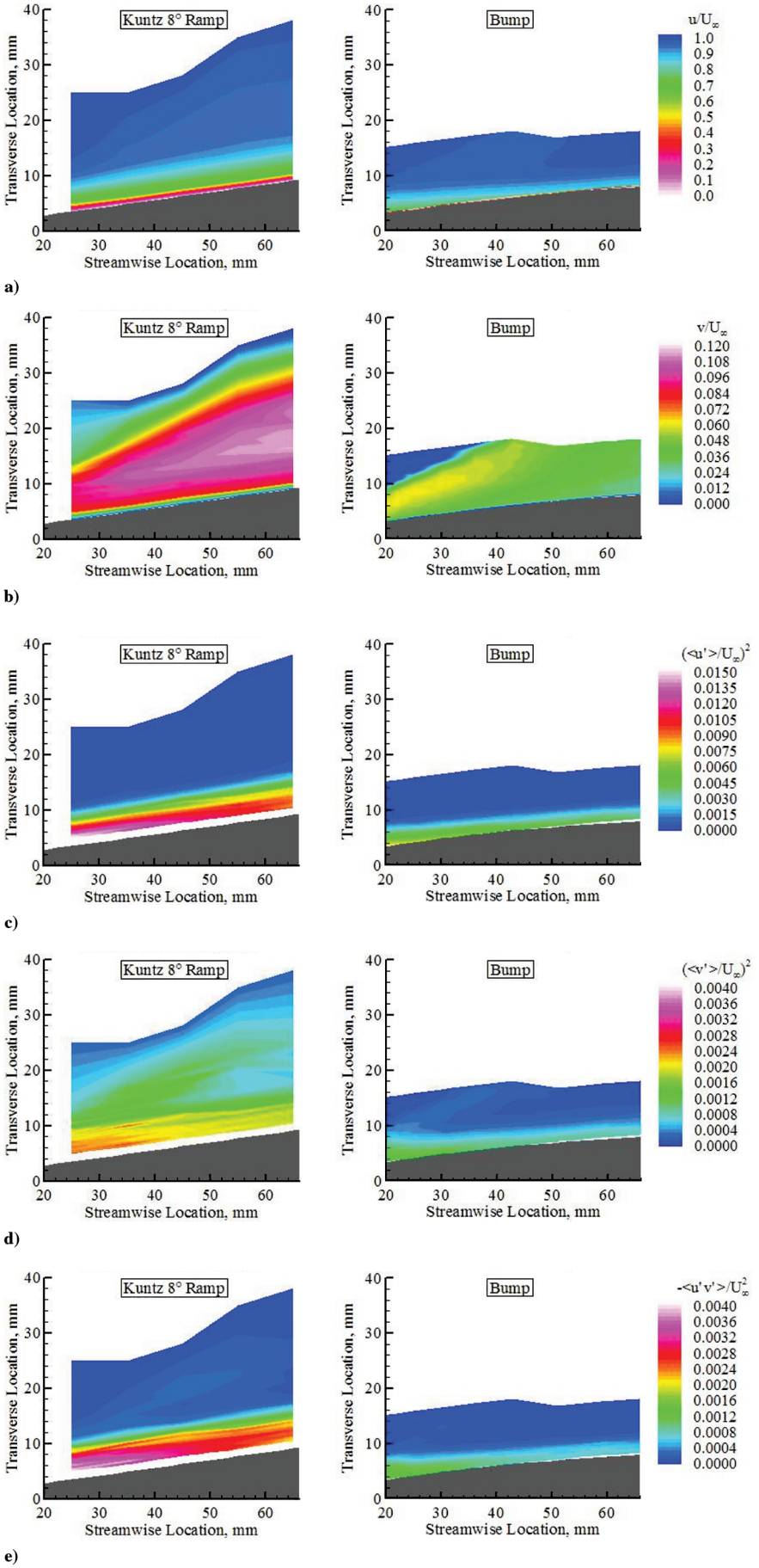

Fig. 17 Comparison of a Kuntz [13] 8 deg ramp with bump-compression results: a) mean streamwise velocity, b) mean transverse velocity, c) streamwise normal stress, d) transverse normal stress, and e) shear stress.

The gaps in data for both Fig. 12 and the $x = 25.4$ mm distribution of Fig. 13 are due to shock-skewed mean velocity profiles, which prevented accurate estimation of boundary-layer thicknesses at these locations.

D. Experimental Comparison with Two-Dimensional Ramp Compression Studies

To evaluate the significance of the spanwise geometry variation and relate it to a canonical compression flow, a comparison is made between the current three-dimensional bump flowfield and that of a two-dimensional ramp. Many research investigations have addressed 2-D compression-ramps flowfields [13–17], with an excellent bibliography and summary of the current state and future areas of compression-ramp research provided by Dolling [18]. The compression-ramp work chosen for comparison here is that of Kuntz [13,14]. Kuntz's work is optimal here because it was conducted in the same University of Illinois wind tunnel used for the current investigation, allowing for a direct flowfield comparison. The Kuntz study examined compression-ramp angles of 8, 12, 16, 20, and 24 deg at a unit Reynolds number of 35×10^6 m^{-1} with the same incoming boundary layer.

The tunnel-width compression-ramp model studied by Kuntz [13,14] is shown schematically in Fig. 14. A schlieren photograph of the 8 deg ramp flowfield is provided in Fig. 15, with the bump shock angle overlaid in the picture as a white line. Despite having a greater initial inclination angle for the bump surface, it is apparent that the bump shock angle is less steep than for the ramp, and therefore the bump shock is weaker. This is attributed to the gentler overall turning of the flow caused by the bump contour (three-dimensional relief effect) and the associated curved shock structure.

The static pressures measured along the model centerlines for the bump and for the ramp are compared in Fig. 16, along with the inviscid pressure rise for a shock on an 8 deg ramp. Here, it is readily seen that the bump surface yields significantly different flow behavior from the compression ramp. The influence of three-dimensionality and decreasing surface angle of the bump causes a favorable pressure gradient along the majority of the bump model, whereas the 2-D ramp's pressure distribution asymptotes to approximately the value predicted by inviscid oblique shock theory. Although the initial compression levels are similar, the bump shock tends to have reduced standoff distance from the leading edge as compared with the ramp shock, which is shown by the upstream shift of the pressure distribution for the latter case.

A comparison of the mean velocity and turbulent stress fields for these two geometries is made by examining a common region of the flow. Contour plots of the mean velocity and turbulent stress fields are provided in Fig. 17. The ramp compression clearly leads to a much thicker boundary layer and greater mean wall-normal velocities along the model centerline. Significantly higher turbulent stresses are also observed with the ramp flowfield. The three-dimensionality of the bump clearly allows for a much thinner and less turbulent boundary layer to exist along the model centerline. As the flow progresses downstream from the leading edge of the bump, the combined effects of flow expansion and spanwise fluid motion result in the bump boundary layer being thinner and less turbulent than for the ramp flowfield at offcenterline locations as well (Fig. 11).

IV. Conclusions

The compression surface studied here has been shown to generate a curved shock system that, combined with the bump contour itself, yields a highly three-dimensional flowfield. The static pressure field reaches peak compression along the model centerline approximately 10 mm downstream of the leading edge and is then followed by a favorable streamwise gradient that exists for approximately 80 mm. This is accompanied by favorable spanwise-outward pressure gradients that are significant to at least 25.4 mm downstream of the leading edge. There is no evidence that the combined compression/expansion process is accompanied by boundary-layer separation.

The mean velocity behavior varies from that for two-dimensional compression ramps due to the generation of a significant spanwise-outward velocity component in the flowfield caused by the spanwise pressure gradient (as evidenced by the surface-flow visualization and static pressure measurements). The measured centerline mean streamwise velocity shows a significant thinning of the boundary layer downstream of the shock wave. However, the offcenterline boundary layer is found to thicken substantially, indicating that the bump causes boundary-layer fluid to be pushed away from the centerline toward the sides of the bump. Along the centerline, the transverse velocity behind the shock and directly over the bump shows significant upward deflection and then realignment to the streamwise direction, which is consistent with the increasing and then decreasing surface angularity.

The turbulent stresses are all increased greatly in the region immediately downstream of the shock. The centerline streamwise normal, transverse normal, and shear stresses tend to substantially decrease in magnitude as the flow moves over the bump centerline, indicating that the boundary layer is recovering significantly. However, the offcenterline turbulent stresses at the bump sides tend to maintain high postshock levels, even at the furthest downstream measurement plane (more than $7\delta_0$ downstream). These results are attributed to the combination of favorable flow expansion on the bump centerline and the transfer of low-momentum boundary-layer fluid to the sides of the bump (due to the spanwise-outward velocity component). The three-dimensionality of the bump flowfield is therefore preferable to a similar 2-D compression-ramp flowfield from the standpoint of boundary-layer turbulence and thickness on the bump surface. The thick region of low-momentum boundary-layer fluid to the sides of the bump can be minimized in inlet applications by a well-placed cowl system to avoid its ingestion.

Ideas for extension of this work include the following:

1) Use flow management devices (e.g., bleed, vortex generators, etc.) in an attempt to extend the thin portion of the boundary layer to greater spanwise extents.

2) Introduce an impinging oblique shock into the bump flowfield to simulate the presence of a cowl placed above the bump.

Acknowledgments

The bump-compression model and funding for this research were provided by Boeing Phantom Works in St. Louis, Missouri. The support, supervision, and advice from Boeing's Paul Devereaux and Mary Peter are gratefully acknowledged.

References

[1] Hamed, A., and Shang, J. S., "Survey of Validation Data Base for Shockwave Boundary-Layer Interactions in Supersonic Inlets," *Journal of Propulsion and Power*, Vol. 7, No. 4, 1991, pp. 617–625. doi:10.2514/3.23370

[2] Simon, P. C., Dennis, W. B., and Huff, R. G., "Performance of External-Compression Bump Inlet at Mach Numbers of 1.5 to 2.0," NACA RM E56L19, 1957.

[3] Seddon, J., and Goldsmith, E. L., *Intake Aerodynamics*, Collins Professional and Technical Books, London, 1985.

[4] Ferri, A., "Supersonic Flow Around Circular Cones at Angles of Attack," NACA Rept. 1045, 1951.

[5] Gridley, M. C., and Cahill, M. J., "ACIS Air Induction System Trade Study," *ASME/SAE/ASEE Joint Propulsion Conference and Exhibit*, AIAA Paper 1996-2646, Lake Buena Vista, FL, 1996.

[6] Gridley, M. C., and Walker, S. H., "Inlet and Nozzle Technology for 21st Century Fighter Aircraft," American Society of Mechanical Engineers Paper 96-GT-244, 1996.

[7] Hamstra, J. W., McCallum, B. N., Sylvester, T. G., Denner, B. W., and Moorehouse, J. A., "Transition Shoulder System and Method for Diverting Boundary Layer Air," U.S. Patent 5,749,542, 1998.

[8] Hamstra, J. W., and Sylvester, G. S., "System and Method for Diverting Boundary Layer Air," U.S. Patent 5,779,189, 1998.

[9] Hehs, E., "JSF Diverterless Supersonic Inlet," *Code One Magazine*, Vol. 15, No. 3, July 2000; available online at http://www.codeonemagazine.com/archives/2000/articles/july_00/divertless_1.html [retrieved 25 Jan. 2009].

[10] Hamstra, J. W., McCallum, B. N., McFarlan, J. D., and Moorehouse, J. A., "Development, Verification, and Transition of an Advanced Engine Inlet Concept for Combat Aircraft Application," Lockheed Martin Aerospace Corp. Paper MP-121-P-43, 2003.

[11] Bloomberg, J. E., "An Investigation of Particle Dynamics Effects Related to LDV Measurements in Compressible Flows," M.S. Thesis, Univ. of Illinois at Urbana–Champaign, Urbana, IL, 1989.

[12] Sun, C.-C., and Childs, M. E., "A Modified Wall Wake Velocity Profile for Turbulent Compressible Boundary Layers," *Journal of Aircraft*, Vol. 10, No. 6, 1973, pp. 381–383.
doi:10.2514/3.44376

[13] Kuntz, D. W., "An Experimental Investigation of the Shock Wave-Turbulent Boundary Layer Interaction," Ph.D. Thesis, Univ. of Illinois at Urbana–Champaign, Urbana, IL, 1985.

[14] Kuntz, D. W., Amatucci, V. A., and Addy, A. L., "Turbulent Boundary-Layer Properties Downstream of the Shock-Wave/Boundary-Layer Interaction," *AIAA Journal*, Vol. 25, No. 5, 1987, pp. 668–675.
doi:10.2514/3.9681

[15] Ardonceau, P. L., "The Structure of Turbulence in a Supersonic Shock-Wave/Boundary-Layer Interaction," *AIAA Journal*, Vol. 22, No. 9, 1984, pp. 1254–1262.
doi:10.2514/3.48565

[16] Settles, G. S., Fitzpatrick, T. J., and Bogdonoff, S. M., "Detailed Study of Attached and Separated Compression Corner Flowfields in High Reynolds Number Supersonic Flow," *AIAA Journal*, Vol. 17, No. 6, 1979, pp. 579–585.
doi:10.2514/3.61180

[17] Smits, A. J., and Muck, K. C., "Experimental Study of Three Shock Wave/Turbulent Boundary Layer Interactions," *Journal of Fluid Mechanics*, Vol. 182, No. -1, 1987, pp. 291–314.
doi:10.1017/S0022112087002349

[18] Dolling, D. S., "Fifty Years of Shock-Wave/Boundary-Layer Interaction Research: What Next?," *AIAA Journal*, Vol. 39, No. 8, 2001, pp. 1517–1531.
doi:10.2514/2.1476

F. Liu
Associate Editor